Journal of Materials Chemistry A

Three-in-one cathode host based on Nb3O8/graphene superlattice heterostructures for high-performance Li–S batteries

Journal:	*Journal of Materials Chemistry A*
Manuscript ID	TA-ART-03-2021-001913.R1
Article Type:	Paper
Date Submitted by the Author:	26-Mar-2021
Complete List of Authors:	WANG, Chenhui; National Institute for Materials Science, Soft Chemistry Group Sakai, Nobuyuki; National Institute for Materials Sciencea, Soft Chemistry Group, MANA Ebina, Yasuo; National Institute for Materials Science, Soft Chemistry Group KIKUCHI, Takayuki; National Institute for Materials Science, Soft chemistry group Snowdon, Monika; University of Waterloo, Chemistry Tang, Dai-Ming; National Institute for Materials Science (NIMS), WPI International Center for Materials Nanoarchitectonics (MANA) Ma, Renzhi; National Institute for Materials Science, Soft Chemistry Group, Advanced Materials Laboratory Sasaki, Takayoshi; National Institute of Materials Science, International Center for Materials Nanoarchitectonics

SCHOLARONE™
Manuscripts

ARTICLE

Three-in-one cathode host based on Nb_3O_8/graphene superlattice heterostructures for high-performance Li–S batteries

Received 00th January 20xx,
Accepted 00th January 20xx

DOI: 10.1039/x0xx00000x

Chenhui Wang[a], Nobuyuki Sakai[a], Yasuo Ebina[a], Takayuki Kikuchi[a], Monika R. Snowdon[b], Daiming Tang[a], Renzhi Ma[a], and Takayoshi Sasaki[a]*

Lithium-sulfur batteries have high promise for applications in next-generation energy storage. However, further advances have been hindered by various intractable challenges, particularly three notorious problems: the "shuttle effect", sluggish kinetics of lithium polysulfide conversion, and nonuniform nucleation of Li_2S. In this study, a three-in-one cathode host based on a superlattice of two-dimensional (2D) materials is designed to tackle these three issues. Alternately restacked Nb_3O_8 nanosheets with Lewis acid surface and reduced graphene oxide (rGO) with high electrical conductivity give rise to a unique superlattice structure without the self-restacking, thereby maximizing the synergistic effect that stems from the inherent advantages of each component. The Nb_3O_8/rGO superlattice cathode host is characterized by its high affinity, excellent catalytic activity, abundance of exposed active sites, and high electrical conductivity, effectively confining lithium polysulfides and reducing the overpotentials for lithium polysulfide conversion and Li_2S nucleation. As a result, high-performance lithium-sulfur batteries were achieved with an initial capacity of 1529 mAh g^{-1} at 0.1 C and a slow capacity decay of 0.064% per cycle at 1 C over 1000 cycles. This work provides a novel strategy of heteroassembling 2D nanosheets as a cathode host, opening a promising avenue for advanced lithium-sulfur batteries.

Introduction

The evolution of smaller, smarter, swifter, and more secure electronic devices urgently needs next-generation energy storage systems with higher energy density and power density, as well as longer life spans.[1] Thus, the development of advanced batteries beyond lithium-ion batteries, which have been one of the most widely used energy storage systems in mobile electronic devices for decades, has been stimulated to meet the above requirements.[2-5] Lithium-sulfur batteries with much higher theoretical energy densities (S: 1675 mAh g^{-1} and Li: 3860 mAh g^{-1}) have been highly regarded as promising candidates for next-generation energy storage technology.[6-9] However, many challenges need to be overcome before their use in practical applications.[10, 11] The challenges derived from positive half-cells are intractable and complex, such as their low Coulombic efficiency and rapid capacity fade caused by the "shuttle effect", high polarization resulting from the low electrical conductivity of sulfur, large volume changes during charge/discharge processes, sluggish conversion kinetics of lithium polysulfides and nonuniform deposition of Li_2S. Thus, high-performance cathodes have been designed and fabricated for the development of lithium-sulfur batteries with the prospect of their wide use in practical applications.[12-14]

In the early research period, carbon materials with various morphologies, structures, and pore sizes were carefully designed to relieve the "shuttle effect" by physically adsorbing or retaining lithium polysulfides.[15-18] However, physical adsorption and reservoirs are limited by the weak interaction between carbon materials and lithium polysulfides. Later, polar materials capable of forming chemical bonds with lithium polysulfides, such as metal oxides,[19-22] metal nitrides,[23] and metal chalcogenides,[24, 25] were developed to confine lithium polysulfides. Moreover, the surface properties, electronic structure, adsorption energy, and lattice defects of these materials have been carefully controlled to accelerate the conversion of lithium polysulfides, which can reduce the electrochemical polarization of lithium-sulfur batteries. On the basis of acid-base theory, various materials with Lewis acid surface have been expected to be excellent catalysts for the conversion reaction of lithium polysulfides, which are regarded as Lewis bases with low electronegativity.[26, 27] A layered niobate acid, HNb_3O_8, has been reported to show high catalytic activity for the conversion reaction of lithium polysulfides.[28] Nevertheless, oxygen vacancies exert a negative influence on catalytic activity. Therefore, other approaches are needed to design cathode host materials for high-performance lithium-sulfur batteries. It is also important to note that Li_2S electrodeposition constitutes 50% of the total capacity of lithium-sulfur batteries, which is largely influenced by the morphology and structure of host materials. Hence, a variety of ingenious structures have been designed to improve the

[a] International Center for Materials Nanoarchitectonics (WPI-MANA), National Institute for Materials Science (NIMS), Namiki 1-1, Tsukuba, Ibaraki, 305-0044, Japan. E-mail: SASAKI.Takayoshi@nims.go.jp
[b] Department of Chemistry, Faculty of Science, Waterloo Institute of Nanotechnology, University of Waterloo, Waterloo, ON, N2L 3G1, Canada.
Electronic Supplementary Information (ESI) available: Experimental section, supplementary figures, and Tables. See DOI: 10.1039/x0xx00000x

uniformity of the Li_2S electrodeposition layer, which helps to further reduce battery polarization and improve the utilization of sulfur.[29, 30]

A wide variety of 2D materials has been reported. Their intriguing properties have been revealed and various promising applications have been proposed.[31-35] 2D materials are characterized by an extremely high aspect ratio, which provides a high specific surface area and an abundance of 2D diffusion channels for the adsorption and conversion of lithium polysulfides, Li_2S nucleation, and mass transfer to reduce the polarization of lithium-sulfur batteries.[36-38] In particular, single-layer nanosheets obtained by chemical exfoliation can approach a molecular scale thickness with the maximum number of active sites, suggesting their promising application in lithium-sulfur batteries.[39-41] As single-layer metal oxide nanosheets with the Lewis acid surface may contribute to superior activity in regard to the conversion reaction of lithium polysulfides, they are very promising building blocks for high-performance cathodes in lithium-sulfur batteries. However, it is crucial to overcome the easy restacking tendency of 2D materials, as well as the low electrical conductivity of metal oxides and sulfur. Recently heteroassembly of multiple 2D nanosheets has attracted enormous attention because resulting superlattice assemblies provide great opportunities to realize new and advanced functionalities.[42-49] Particularly, the construction of composites based on single-layer metal oxide nanosheets and other counterpart materials with high electrical conductivity has been proven very effective towards superior electrochemical energy storage and conversion.[50-56] A molecular-level assembly may fully highlight the properties of each component to achieve synergistic effects,[57-63] however, this strategy has not been applied to yield a highly efficient multifunctional cathode host for lithium-sulfur batteries.

In this study, unilamellar Nb_3O_8 nanosheets with polar Nb-O bonds, the Lewis acid surface, and highly exposed active sites are hybridized with reduced graphene oxide (rGO) nanosheets with high electrical conductivity to design a three-in-one cathode host for high-performance lithium-sulfur batteries. This host achieves three functions: prevents the shuttle effect, accelerates lithium polysulfide conversion, and promotes Li_2S nucleation. By the electrostatic flocculation process, negatively charged Nb_3O_8 nanosheets and positively charged PDDA-modified rGO were alternately restacked to construct Nb_3O_8/rGO superlattice heterostructures (S-Nb_3O_8/rGO).[64] Compared with an aggregate of self-restacked individual nanosheets and a composite of randomly restacked Nb_3O_8 and rGO, the Nb_3O_8/rGO superlattice heterostructure showed the highest affinity to lithium polysulfides, highest catalytic activity for the lithium polysulfide conversion reaction, and excellent Li_2S deposition capacity, thereby leading to the best battery performance. The superior performance of this superlattice structure attests to the high potential of heteroassembling 2D nanosheets for the development of lithium-sulfur batteries.

Results and discussion

The superlattice composite of alternately restacked monolayer Nb_3O_8 nanosheets and rGO (S-Nb_3O_8/rGO) was fabricated by the electrostatic charge-driven flocculation method **(Scheme 1a)**, wherein the suspensions of negatively charged Nb_3O_8 nanosheets and positively charged PAAD-modified rGO were dropwise added to water. Via electrostatic self-assembly, these oppositely charged materials were alternately restacked to produce the superlattice assembly.[65, 66] For comparison, single component aggregates of Nb_3O_8 nanosheets and PDDA-modified rGO were prepared by directly freeze-drying their respective suspensions. A composite with randomly restacked Nb_3O_8 nanosheets and rGO (R-Nb_3O_8/rGO) was also prepared by directly adding the suspensions of negatively charged Nb_3O_8 nanosheets and original rGO into a PDDA solution. These control samples were employed to demonstrate the merits of the prepared superlattice heterostructures as a three-in-one cathode host for high-performance lithium-sulfur batteries. The preparation processes for the samples are described in detail in the experimental section of the Supporting Information.

The building blocks, namely, the single-layer Nb_3O_8 nanosheets and PDDA-modified rGO nanosheets, were first examined by atomic force microscopy (AFM) after deposited on a silicon substrate. As shown in Figure 1a, the Nb_3O_8 nanosheets show a thickness of ~1.3 nm and a lateral size of several micrometers, confirming their single-layer nature.[67, 68] The thickness of PDDA-modified rGO was ~1.5 nm, while the typical lateral size was several micrometers (Figure 1b). As shown by X-ray diffraction (XRD) in Figure 1c, the restacked Nb_3O_8 showed in-plane diffraction peaks of 240, 080, 400, and $0\bar{1}20$ at 24.6°, 31.4°, 38.7°, and 48.1°, respectively, and the peak at 4.5° indicates an interlayer spacing of 1.97 nm. The in-plane diffraction peaks of Nb_3O_8 also appeared in R-Nb_3O_8/rGO together with a basal peak

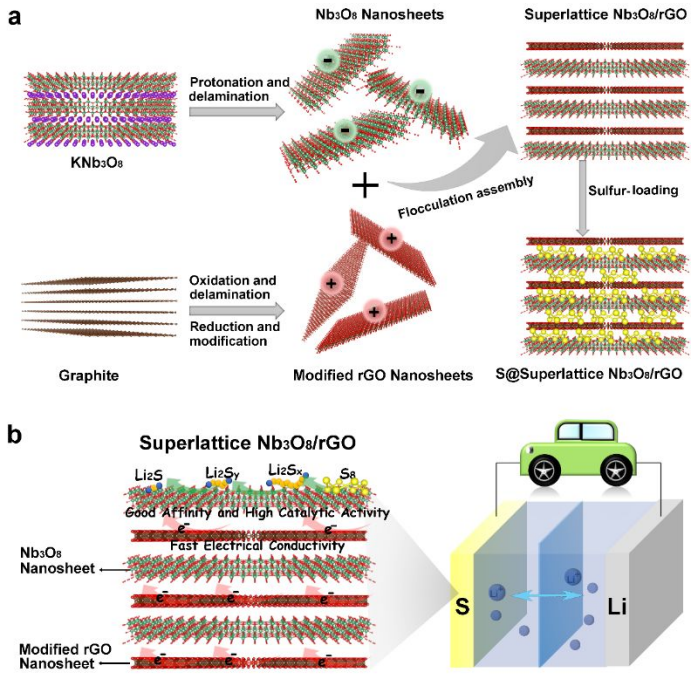

Scheme 1. Schematic illustration showing a) the preparation of a cathode based on superlattice Nb_3O_8/rGO and b) the advantages of superlattice Nb_3O_8/rGO in lithium-sulfur battery applications.

This journal is © The Royal Society of Chemistry 20xx

Please do not adjust margins

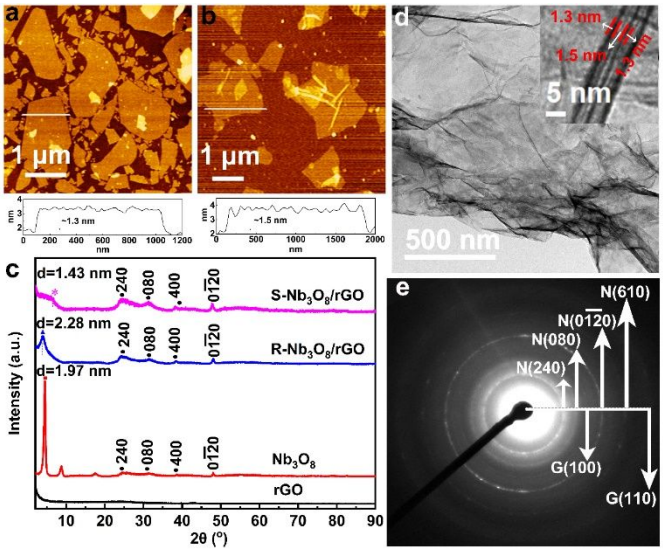

Figure 1. AFM images and height profiles of a) single-layer Nb_3O_8 nanosheets and b) PDDA-modified rGO nanosheets; c) XRD patterns of restacked PDDA-modified rGO, restacked Nb_3O_8, R-Nb_3O_8/rGO and S-Nb_3O_8/rGO; d) TEM images and e) SAED pattern of S-Nb_3O_8/rGO.

at 2.28 nm. S-Nb_3O_8/rGO also showed the same in-plane diffraction peaks as Nb_3O_8, whereas a broad diffraction peak centered at 6.2° indicates an interlayer spacing of 1.43 nm. This peak may be ascribed to the (002) diffraction of the superlattice structure of S-Nb_3O_8/rGO, which equals approximately half of the total thickness of Nb_3O_8 (1.3 nm) and PDDA-modified rGO (1.5 nm), suggesting that S-Nb_3O_8/rGO has a periodic superlattice structure. This structure is formed due to the opposite surface charges of the two different nanosheets, effectively preventing the self-restacking into a single nanosheet component. The microstructure of S-Nb_3O_8/rGO was examined by transmission electron microscopy (TEM). As shown in Figure 1d, S-Nb_3O_8/rGO showed a very thin lamellar structure with a lateral size on the micrometer scale. Lattice fringes with spacings of 1.3 and 1.5 nm directly neighboring each other were observed (inset of Figure 1d), agreeing well with the thicknesses of the Nb_3O_8 nanosheets and PDDA-modified rGO, respectively. Moreover, the in-plane diffraction rings of the Nb_3O_8 and rGO nanosheets identified by selected area electron diffraction (SAED) verify the intimate restacking of the Nb_3O_8 nanosheets and rGO (Figure 1e). As shown in Figure S1, the porosity of S-Nb_3O_8/rGO is apparent. The energy-dispersive X-ray spectroscopy (EDS) elemental mapping results indicate the homogenous distribution of C, O, and Nb, again suggesting the intact assembly of Nb_3O_8 nanosheets and rGO into a superlattice structure (Figure S2).

S-Nb_3O_8/rGO was examined by thermogravimetric and differential thermal analysis (TG-DTA) in an ambient atmosphere. The thermal stability of the Nb_3O_8 nanosheets was initially studied as a reference. As shown in Figure S3, the weight loss below 200 °C may be ascribed to the removal of water, and the endothermic event above 200 °C may correspond to the decomposition of the accommodated TBA^+. On the other hand, the weight loss above 200 °C for the S-Nb_3O_8/rGO recorded in Figure S4 is attributed to the combustion of rGO. Based on the TG results, the mass ratio of rGO to Nb_3O_8 in S-Nb_3O_8/rGO is estimated to be 0.256, which is a little larger than the theoretical value based on the hypothetical area-matching model (0.185). This small difference may be caused by the PDDA in S-Nb_3O_8/rGO. The detailed calculation is described in the experimental section of the Supporting Information.

The catalytic activity of the samples to the lithium polysulfide conversion reaction was examined by electrochemical tests with a Li_2S_6 symmetric battery. Cyclic voltammetry (CV) of the blank symmetric batteries, which were assembled with blank electrolyte without Li_2S_6, was tested to extract the possible influence of the electrochemical activity of host materials. As shown in Figures S5-8, compared to the corresponding Li_2S_6 symmetric battery, the response current of the blank symmetric batteries was very small, confirming the negligible effect of the electrochemical activity of the host materials. As depicted in Figure 2a, two redox peaks in the CV curve of rGO suggest a two-step electrochemical reaction, which may be ascribed to the conversion of Li_2S_6/Li_2S_4 (-0.38 V/-0.12 V) and Li_2S_8/Li_2S_6 (0.09 V/0.32 V).[69] The Nb_3O_8 nanosheets exhibited an abnormally low response current, which may be due to the low electrical conductivity and large ohmic resistance. The electrochemical impedance spectroscopy (EIS) results support the extremely high resistance of Nb_3O_8 compared to other samples (Figure S9). Only one apparent couple of redox peaks was recognized in R-Nb_3O_8/rGO and S-Nb_3O_8/rGO, inferring that the Li_2S_6/Li_2S_4 and Li_2S_8/Li_2S_6 reactions overlap. This overlap may result from the low electronic conductivity of Nb_3O_8 in R-Nb_3O_8/rGO and S-Nb_3O_8/rGO. The redox current densities of the composites (R-Nb_3O_8/rGO and S-Nb_3O_8/rGO) were higher than the single component (restacked rGO and restacked Nb_3O_8) samples, validating the advantages of combining Nb_3O_8 nanosheets and

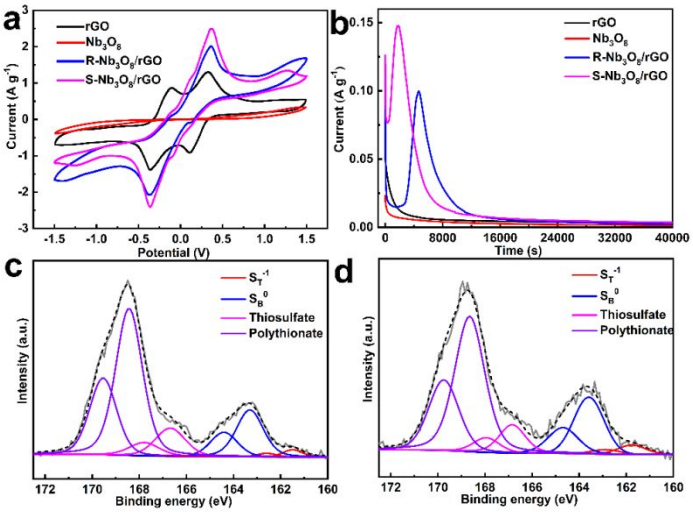

Figure 2. a) CV curves of rGO, Nb_3O_8 nanosheet, R-Nb_3O_8/rGO and S-Nb_3O_8/rGO in Li_2S_6 symmetric battery at a scan rate of 1 mV s^{-1}; b) current vs. time curve of rGO, Nb_3O_8 nanosheet, R-Nb_3O_8/rGO and S-Nb_3O_8/rGO in Li_2S_8 battery at a constant potential of 2.05 V; and XPS curve fitting of the high-resolution S 2p spectra of the c) R-Nb_3O_8/rGO and d) S-Nb_3O_8/rGO electrodes after the potentiostatic process.

rGO to improve the catalytic activity for converting lithium polysulfides. On the one hand, the Lewis acid surface of Nb_3O_8 and its high affinity to lithium polysulfides are beneficial for enhancing the catalytic activity for the lithium polysulfide conversion reaction. On the other hand, the high electrical conductivity of rGO is helpful to reduce the ohmic resistance. As a result, the composite materials (R-Nb_3O_8/rGO and S-Nb_3O_8/rGO) achieved higher electrical conductivity than Nb_3O_8 and better catalytic activity than rGO, thus exhibiting much higher activity for the lithium polysulfide conversion reaction. Furthermore, the electrochemical activity of S-Nb_3O_8/rGO was higher than R-Nb_3O_8/rGO, providing strong evidence for the effectiveness of constructing a superlattice structure to maximize the advantages of two components and achieving an ideal synergistic effect. The self-restacking of either Nb_3O_8 or rGO may occur in R-Nb_3O_8/rGO, resulting in low homogeneity and offsetting the synergistic effect of the heteroassembled Nb_3O_8 and rGO. In contrast, the self-restacking problem is efficiently hindered in S-Nb_3O_8/rGO, owing to the control for the opposite surface charge. The intimate and maximum contact of rGO and Nb_3O_8 at the molecular scale leads to high electrical conductivity and provides more exposed active sites for the adsorption and conversion of lithium polysulfides. Profiting from the superlattice heterostructure and the maximum synergistic effect of Nb_3O_8 and rGO, the highest catalytic activity for the lithium polysulfide conversion reaction is achieved by S-Nb_3O_8/rGO. In addition, the superlattice Nb_3O_8/rGO heterostructure efficiently overcomes the "shuttle effect". The adsorption capacity of lithium polysulfides is shown in Figures S10-11. The light color or low optical absorption of the Li_2S_6 solution after mixing with S-Nb_3O_8/rGO indicates its larger adsorption capacity than that of R-Nb_3O_8/rGO. S-Nb_3O_8/rGO may efficiently overcome the "shuttle effect" through bifunctional chemical bonding and physical confinement, wherein lithium polysulfides are chemically bonded to the exposed sites and physically confined in the interlayer of the layered structure of alternately restacked Nb_3O_8 and rGO.

As another important process of lithium-sulfur batteries, the solid nucleation process was examined by potentiostatic techniques. The current *vs.* time curves of samples in the potentiostatic process (Figure 2b) can be classified into two groups. One group is for the composite materials, R-Nb_3O_8/rGO and S-Nb_3O_8/rGO. These composites showed three regions where the current first decreased, then a peak appeared, and finally leveled off to a constant current over time. The other group is for the single-component materials, rGO and Nb_3O_8, which only exhibited the first and third regions. The first region of decreasing current in all samples is ascribed to the liquid-liquid conversion process of soluble long-chain lithium polysulfides to soluble short-chain polysulfides.[70] In this process, the reactant concentration of soluble long-chain lithium polysulfides near the electrode surface decreases as the reaction continues, resulting in a decreasing current over time. The second peak region observed for R-Nb_3O_8/rGO and S-Nb_3O_8/rGO is ascribed to the nucleation of solid Li_2S or Li_2S_2, wherein the current first increases with the nucleation reaction process and then decreases by its gradual suppression.[71] The coverage of deposited Li_2S or Li_2S_2 with low electrical conductivity decreases the number of nucleation sites and increases the electrochemical polarization, thereby suppressing the nucleation reaction at a constant potential. The third region that shows the current leveling off in all samples may be ascribed to the conversion reaction of the soluble lithium polysulfides in the diffusion control region. Thus, the two-region process observed for rGO and Nb_3O_8 suggests that the solid nucleation reaction does not take place on rGO and Nb_3O_8 at this constant potential, while the three-region process indicates the occurrence of a solid nucleation reaction on R-Nb_3O_8/rGO and S-Nb_3O_8/rGO at the same constant potential.

After the potentiostatic process, the electrodes were characterized to understand the effects. A peak at 435 cm^{-1} ascribed to Li_2S_2 appeared in the Raman spectra of R-Nb_3O_8/rGO and S-Nb_3O_8/rGO, thereby supporting this interpretation of the occurrence of the solid nucleation reactions on R-Nb_3O_8/rGO and S-Nb_3O_8/rGO (Figure S12). The results suggest that the low nucleation activity of pristine rGO and the high electrical resistivity of Nb_3O_8 lead to solid nucleation on rGO and Nb_3O_8 having a higher overpotential than on R-Nb_3O_8/rGO and S-Nb_3O_8/rGO. Additionally, the appearance of a nucleation peak in shorter time on S-Nb_3O_8/rGO (1778 s) than on R-Nb_3O_8/rGO (4672 s) indicates the faster nucleation rate on the former. The deposition capacity of S-Nb_3O_8/rGO (447 C g^{-1}), which is calculated from the peak area, is larger than that of R-Nb_3O_8/rGO (276 C g^{-1}), indicating more exposed nucleation sites and a more uniform distribution of Li_2S or Li_2S_2 on S-Nb_3O_8/rGO. The uniform deposition of Li_2S was verified by the homogeneous distribution of S by EDS mapping for the S-Nb_3O_8/rGO electrode after the potentiostatic process (Figure S13). Notably, the electrochemical impedance of S-Nb_3O_8/rGO is still the smallest among the samples even after the mass deposition of Li_2S or Li_2S_2 with low electrical conductivity (Figure S14), again supporting the result that Li_2S or Li_2S_2 forms a uniform coating due to the fast deposition kinetics and largely exposed deposition sites on S-Nb_3O_8/rGO. The chemical state and composition of sulfur on R-Nb_3O_8/rGO and S-Nb_3O_8/rGO after the potentiostatic process were examined by X-ray photoelectron spectroscopy (XPS) to monitor the nucleation performance. The S 2p XPS spectra of R-Nb_3O_8/rGO and S-Nb_3O_8/rGO (Figure 2c and d) show a similar profile composed of four peaks at ~161.6 eV, ~163.4 eV, ~166.8 eV, and ~168.5 eV. The peak at ~161.6 eV may be assigned to the terminal S (S_T^{-1}) of lithium polysulfide and Li_2S, while the peak at ~163.4 eV is ascribed to the bridging S (S_B^0) of lithium polysulfide.[72, 73] The high ratio of S_T^{-1}/S_B^0 indicates the high content of short-chain lithium polysulfides and Li_2S. Thiosulfate (~166.8 eV) and polythionate complexes (~168.5 eV) may be formed by the reaction of lithium polysulfides with the carboxyl and hydroxyl groups on rGO, which involve the conversion of lithium polysulfides to thiosulfate and polythionate complex species.[74] The composition of sulfur species is summarized in **Table 1**. The S_T^{-1}/S_B^0 ratio of S-Nb_3O_8/rGO (17%) is higher than that of R-Nb_3O_8/rGO (11%), indicating a higher content of short-chain lithium polysulfides and Li_2S on S-Nb_3O_8/rGO after the

This journal is © The Royal Society of Chemistry 20xx

Please do not adjust margins

Table 1. Compositions of sulfur species in R-Nb_3O_8/rGO and S-Nb_3O_8/rGO electrodes after potentiostatic process revealed by high resolution S2p XPS spectra.

Materials	S_T^{-1} [%][a)]	S_B^0 [%][b)]	Thiosulfate [%]	Polythionate [%]
R-Nb_3O_8/rGO	2.24	20.3	13.2	64.2
S-Nb_3O_8/rGO	3.89	22.8	11.2	62.0

[a)] Terminal S; [b)] Bridging S.

potentiostatic process, which is consistent with the performance of Li_2S nucleation observed on S-Nb_3O_8/rGO being higher than that on R-Nb_3O_8/rGO. The excellent Li_2S nucleation performance of S-Nb_3O_8/rGO may be related to the superlattice heterostructure, which provides a fast mass transfer channel and electron conductive path, high affinity to lithium polysulfide, and many exposed adsorption and nucleation sites. In this way, lithium polysulfides migrate effectively through the two-dimensional channels created by the layered structure of alternately restacked Nb_3O_8 and rGO nanosheets, and the lithium polysulfides are adsorbed on the exposed sites that are uniformly distributed on Nb_3O_8, leading to the uniform deposition of Li_2S via fast electron transfer along the directly neighboring rGO. In conclusion, S-Nb_3O_8/rGO is a promising three-in-one multifunctional cathode host material for high-performance lithium-sulfur batteries (**Scheme 1b**), synergically integrating the advantages of both materials to overcome the "shuttle effect", attain high catalytic activity for the lithium polysulfide conversion reaction, and provide excellent Li_2S nucleation performance.

Sulfur cathode materials based on different host materials were prepared by the thermal melting method.[75] The S content of all prepared sulfur cathode materials was ~70%, as estimated from the TG results (Figure S15-18). The inclusion of sulfur was confirmed from XRD data (Figure 3a). The diffraction peaks ascribed to S appear were detected in all patterns, together with the basal diffraction peaks of Nb_3O_8. Slight shrinkage in the basal spacing was observed (Nb_3O_8: 1.93 nm *vs.* S@Nb_3O_8: 1.74 nm and R-Nb_3O_8/rGO: 2.28 nm *vs.* S@R-Nb_3O_8/rGO: 2.13 nm), which may be due to the loss of interlayer water during the preparation of sulfur electrode materials (Figures S16-17). In contrast, the interlayer expansion of S-Nb_3O_8/rGO from 1.43 nm to 2.01 nm strongly suggests the insertion of S into the interlayer gallery (Figure 3b). The superlattice structure composed of alternately restacked rGO and Nb_3O_8 nanosheets may promote the diffusion of melted S into the 2D galleries, contributing to the uniform distribution of S. Once the intercalated S transforms to lithium polysulfides, the lithium polysulfides will be efficiently confined in the interlayer space, overcoming the "shuttle effect". Raman spectra were recorded to gain in-depth insight (Figure 3c-f). The peaks at 1345 and 1581 cm^{-1} are identified as the D and G bands of rGO, respectively.[76, 77] The Raman spectra of S show two sharp peaks at 220 cm^{-1} (A_1) and 473 cm^{-1} (A_1 and E_2) (Figure S19). The peaks of S and rGO are identified in the Raman spectra of S@rGO without a peak shift, suggesting no chemical interaction between them in the thermal melting process (Figure 3c, S19).[78, 79] The samples of S@Nb_3O_8 and S@R-Nb_3O_8/rGO showed a similar change as S@rGO (Figures 3d-e and S19), while

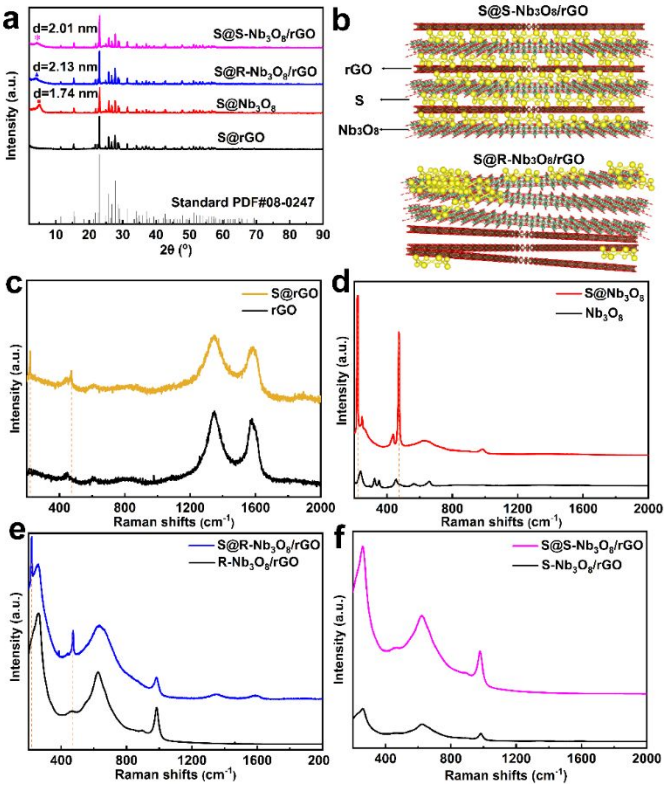

Figure 3. a) XRD patterns of S@rGO, S@Nb_3O_8, S@R-Nb_3O_8/rGO and S@S-Nb_3O_8/rGO; b) Schematic illustration of S@R-Nb_3O_8/rGO and S@S-Nb_3O_8/rGO; Raman spectra of c) rGO and S@rGO, d) Nb_3O_8 and S@Nb_3O_8, e) R-Nb_3O_8/rGO and S@R-Nb_3O_8/rGO, and f) S-Nb_3O_8/rGO and S@S-Nb_3O_8/rGO.

peaks ascribed to S disappeared with S@S-Nb_3O_8/rGO, providing additional evidence for the uniform distribution of sulfur (Figures 3f and S19).

Finally, the electrochemical performance of the prepared electrodes in lithium-sulfur batteries was studied. All CV curves showed a similar shape (Figure 4a), suggesting all samples have a similar reaction mechanism. As the potential was swept in the negative direction, two reduction peaks appeared, which may be ascribed to the reduction of S_8 to soluble lithium polysulfides (Li_2S_n, $2 < n < 8$) at ~2.35 V and then to insoluble lithium sulfide (Li_2S, Li_2S_2) at ~2.05 V. The subsequent potential scan in the positive direction showed two oxidation peaks, corresponding to the reverse reactions. Among all samples, the highest peak current was observed with S@S-Nb_3O_8/rGO, indicating its fast reaction kinetics of S_8 to soluble lithium polysulfides and further to insoluble lithium sulfide; this result agrees with the electrochemical results of the Li_2S_6 symmetric and Li_2S_8 batteries (Figure 2a and b). The lowest charge transfer resistance in S@S-Nb_3O_8/rGO further verifies the fast reaction kinetics of S@S-Nb_3O_8/rGO (Figure 4b). The diffusion rates of Li^+ in the samples were evaluated by CV at different scan rates.[80] The peak current (I_P) increased with an increasing scan rate (Figures S20-27). A linear relationship between I_P and the square root of the scan rate ($v^{1/2}$) indicates the diffusion-controlled reaction, wherein the slope is an indicator of the diffusion rate. The current (I_P) of the four redox peaks of each

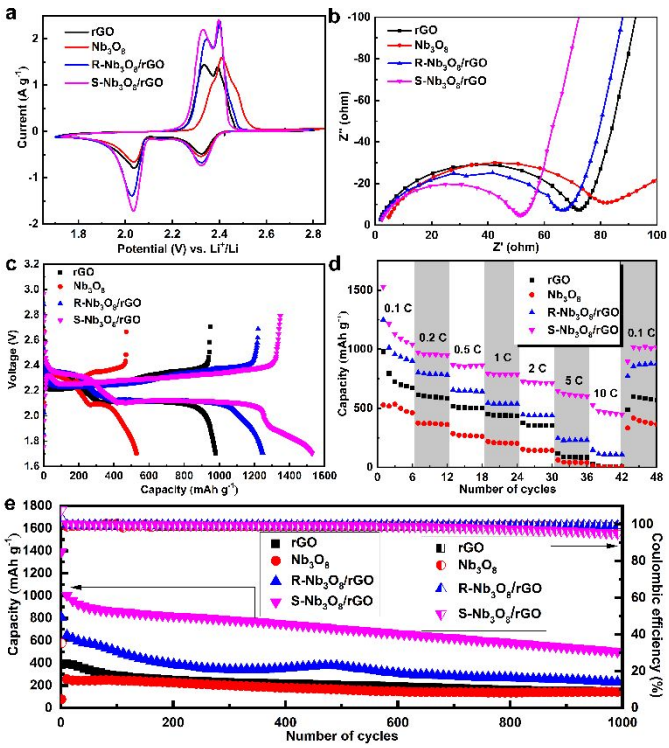

Figure 4. a) CV curves at 0.1 mV s^{-1}, b) EIS curves, c) galvanostatic charge/discharge curves at 0.1 C, d) rate performance, and e) cycling performance at 1 C of the S@rGO, S@Nb_3O_8, S@R-Nb_3O_8/rGO and S@S-Nb_3O_8/rGO Li-S batteries.

Table 2. Slopes of the linear fitting of I_P vs. $v^{1/2}$ from the CV curves of the samples.

Materials	K_{pa1} [A (V s^{-1})$^{-1/2}$][a)]	K_{pa2} [A (V s^{-1})$^{-1/2}$][b)]	K_{pc1} [A (V s^{-1})$^{-1/2}$][c)]	K_{pc2} [A (V s^{-1})$^{-1/2}$][d)]
rGO	0.205	0.186	0.120	0.174
Nb_3O_8	0.192	0.171	0.141	0.113
R-Nb_3O_8/rGO	0.406	0.346	0.226	0.292
S-Nb_3O_8/rGO	0.443	0.418	0.234	0.356

[a)] Slope of the linear fitting of the first anodic peak current (I_{Pa1}) vs. the square root of the scan rate ($v^{1/2}$); [b)] Slope of the linear fitting of the second anodic peak current (I_{Pa2}) vs. the square root of the scan rate ($v^{1/2}$); [c)] Slope of the linear fitting of the first cathodic peak current (I_{Pc1}) vs. the square root of the scan rate ($v^{1/2}$); and [d)] Slope of the linear fitting of the second cathodic peak current (I_{Pc2}) vs. the square root of the scan rate ($v^{1/2}$).

sample were linearly fitted against $v^{1/2}$, and the slopes obtained are listed in Table 2. The slopes of the cathode based on the single-component host materials (S@rGO and S@Nb_3O_8) are much smaller than those of the composite host materials (S@R-Nb_3O_8/rGO and S@S-Nb_3O_8/rGO), indicating the slow Li^+ diffusion rate in the single-component materials during the whole redox process. This result may suggest that the restacked structures from the single-component materials block the Li^+ transport path. The slopes of S@S-Nb_3O_8/rGO are larger than those of S@R-Nb_3O_8/rGO, again verifying the effectiveness of the superlattice structure, which provides a free 2D Li^+ transport path. This structure leads to the high-rate charge/discharge performance of lithium-sulfur batteries.

The electrochemical performance of the materials as the electrodes of lithium-sulfur batteries was also examined by galvanostatic charge/discharge tests. The contribution of host materials to the capacity of lithium-sulfur batteries was negligible (Figure S28). Figure 4c shows two obvious discharge plateaus and one charge plateau in the charge/discharge curves at 0.1 C. During the discharge process, the plateau at ~2.3 V corresponds to the reduction of S_8 to soluble long-chain lithium polysulfides, while the plateau at ~2.1 V corresponds to the further conversion to the solid of short-chain lithium sulfide, which is in agreement with the two reduction peaks in the CV results.[81] The reverse reaction occurs when charging with only one obvious plateau, indicating the larger overpotential for the nucleation of Li_2S. The smallest voltage difference was observed between the charge and discharge plateaus of S@S-Nb_3O_8/rGO, which is especially notable during the latter stage of the charge/discharge process and indicates that S@S-Nb_3O_8/rGO has the smallest battery polarization. This result is due to the acceleration of the reaction kinetics of lithium polysulfide conversion and Li_2S nucleation, contributing to the high utilization of sulfur. The highest discharge capacity of S@S-Nb_3O_8/rGO at a plateau of ~2.3 V results from its good confinement to soluble lithium polysulfides and high catalytic activity for the lithium polysulfide conversion reaction, thereby verifying the validity of this host material design. Furthermore, the largest capacity observed with S@S-Nb_3O_8/rGO at the ~2.1 V plateau is derived from the excellent nucleation performance of insoluble Li_2S_2/Li_2S. The lithium-sulfur battery with S@S-Nb_3O_8/rGO showed the highest initial discharge capacity of 1529 mAh g^{-1} among all the electrodes, demonstrating the superiority of the superlattice heterostructure to reduce the battery polarization and improve sulfur utilization. The rate performance of lithium-sulfur batteries was evaluated from 0.1 C to 10 C (Figure 4d). The lithium-sulfur battery with S@S-Nb_3O_8/rGO delivered discharge capacities of 1529, 975, 867, 793, 726, 647, and 528 mAh g^{-1} at 0.1 C, 0.2 C, 0.5 C, 1 C, 2 C, 5 C, and 10 C, respectively, which are much higher than those with the other electrodes. The lithium-sulfur batteries with S@rGO, S@Nb_3O_8, and S@R-Nb_3O_8/rGO only showed capacities of 115, 62, and 245 mAh g^{-1} at 5 C, respectively. The performance of lithium-sulfur batteries with S@S-Nb_3O_8/rGO is also significant when compared to other recently reported 2D materials, particularly those operated at high rates, which is the key to practical applications (Table S1). The lithium-sulfur battery with S@S-Nb_3O_8/rGO showed excellent cycling performance (Figure 4e), exhibiting a discharge capacity of ~500 mAh g^{-1} after 1000 cycles and a capacity decay of 0.064% per cycle. This high stability may be ascribed to the validity of the chemical and physical bifunctional confinement of the superlattice heterostructure of S-Nb_3O_8/rGO for overcoming the "shuttle effect".

Conclusions

We demonstrated the superiority of the superlattice Nb_3O_8/rGO heterostructure as a three-in-one cathode host material for lithium-sulfur batteries. The lithium-sulfur battery

This journal is © The Royal Society of Chemistry 20xx

Please do not adjust margins

assembled with the designed Nb_3O_8/rGO superlattice heterostructure exhibited an initial specific capacity as high as 1529 mAh g^{-1} at 0.1 C and excellent cycling stability with a capacity decay of 0.064% per cycle over 1000 cycles, even at a high rate of 1 C. On the basis of the structural analysis and electrochemical tests, we conclude that the remarkable battery performance could be attributed to the superlattice Nb_3O_8/rGO heterostructure. The alternate restacking of Nb_3O_8 nanosheets with the Lewis acid surface and rGO with high electrical conductivity provides molecular homogeneity and realizes the physicochemical confinement of lithium polysulfides, high exposure of active sites, superior catalytic activity for the lithium polysulfide conversion and nucleation of Li_2S, and interconnected frameworks and channels for fast transfer of electrons and ions. These results indicate the importance of elaborate structural design to the exceptional synergistic effect of composite electrode materials in achieving multiple functions that enhance sulfur utilization. This work also indicates the promising application of composite electrodes based on 2D materials in lithium-sulfur batteries, which will open up numerous opportunities for the development of next-generation electrochemical energy storage.

Author Contributions

Chenhui Wang: Conceptualization, Methodology, Validation, Investigation, Writing - Original Draft, Writing - Review & Editing, Visualization. **Nobuyuki Sakai:** Writing - Review & Editing. Yasuo **Ebina:** Investigation. **Takayuki Kikuchi**: Investigation. **Monika R. Snowdon**: Investigation. Daiming Tang: Investigation. Renzhi Ma: Writing - Review & Editing. Takayoshi Sasaki: Supervision, Writing - Review & Editing.

Conflicts of interest

There are no conflicts to declare.

Acknowledgements

The authors greatly acknowledge the support of the World Premier International Research Center Initiative on Materials Nanoarchitectonics (WPI-MANA), Education, Culture, Sports, Science and Technology (MEXT), and CREST of the Japan Science and Technology Agency (JST), Japan. The Raman spectra and X-ray photoelectron spectroscopy (XPS) measurements were performed at the Namiki Foundry, National Institute for Materials Science (NIMS) (938, 19-275).

References

1 D. Larcher and J. M. Tarascon, *Nat. Chem.*, 2015, **7**, 19-29.
2 D. Lin, Y. Liu and Y. Cui, *Nat. Nanotechnol.*, 2017, **12**, 194-206.
3 M. M. Thackeray, C. Wolverton and E. D. Isaacs, *Energy Environ. Sci.*, 2012, **5**, 7854-7863.
4 P. Xiong, R. Ma, N. Sakai, L. Nurdiwijayanto and T. Sasaki, *ACS Energy Lett.*, 2018, **3**, 997-1005.
5 P. Xiong, F. Zhang, X. Zhang, S. Wang, H. Liu, B. Sun, J. Zhang, Y. Sun, R. Ma, Y. Bando, C. Zhou, Z. Liu, T. Sasaki and G. Wang, *Nat. Commun.*, 2020, **11**, 3297.
6 P. G. Bruce, S. A. Freunberger, L. J. Hardwick and J. M. Tarascon, *Nat. Mater.*, 2011, **11**, 19-29.
7 W. Xu, J. Wang, F. Ding, X. Chen, E. Nasybulin, Y. Zhang and J.-G. Zhang, *Energy Environ. Sci.*, 2014, **7**, 513-537.
8 A. Manthiram, Y. Fu, S. H. Chung, C. Zu and Y. S. Su, *Chem. Rev.*, 2014, **114**, 11751-11787.
9 A. Manthiram, S. H. Chung and C. Zu, *Adv. Mater.*, 2015, **27**, 1980-2006.
10 Y. X. Yin, S. Xin, Y. G. Guo and L. J. Wan, *Angew. Chem.-Int. Edit.*, 2013, **52**, 13186-13200.
11 S. S. Zhang, *J. Power Sources*, 2013, **231**, 153-162.
12 Y. Yang, G. Zheng and Y. Cui, *Chem Soc Rev*, 2013, **42**, 3018-3032.
13 N. Jayaprakash, J. Shen, S. S. Moganty, A. Corona and L. A. Archer, *Angew. Chem.-Int. Edit.*, 2011, **50**, 5904-5908.
14 L. Ji, M. Rao, H. Zheng, L. Zhang, Y. Li, W. Duan, J. Guo, E. J. Cairns and Y. Zhang, *J. Am. Chem. Soc.*, 2011, **133**, 18522-18525.
15 G. He, B. Mandlmeier, J. Schuster, L. F. Nazar and T. Bein, *Chem. Mater*, 2014, **26**, 3879-3886.
16 G. He, C. J. Hart, X. Liang, A. Garsuch and L. F. Nazar, *ACS Appl. Mater. Interfaces*, 2014, **6**, 10917-10923.
17 X. Ji, K. T. Lee and L. F. Nazar, *Nat Mater*, 2009, **8**, 500-506.
18 X. Ji, S. Evers, R. Black and L. F. Nazar, *Nat. Commun.*, 2011, **2**, 325.
19 H. Yao, G. Zheng, P. C. Hsu, D. Kong, J. J. Cha, W. Li, Z. W. Seh, M. T. McDowell, K. Yan, Z. Liang, V. K. Narasimhan and Y. Cui, *Nat. Commun.*, 2014, **5**, 3943.
20 J. Choi, T.-G. Jeong, D. Lee, S. H. Oh, Y. Jung and Y.-T. Kim, *J. Power Sources*, 2019, **435**, 226707.
21 X. Tao, J. Wang, Z. Ying, Q. Cai, G. Zheng, Y. Gan, H. Huang, Y. Xia, C. Liang, W. Zhang and Y. Cui, *Nano Lett.*, 2014, **14**, 5288-5294.
22 Q. Pang, D. Kundu, M. Cuisinier and L. F. Nazar, *Nat. Commun.*, 2014, **5**, 4759.
23 D. Tian, X. Song, M. Wang, X. Wu, Y. Qiu, B. Guan, X. Xu, L. Fan, N. Zhang and K. Sun, *Adv. Energy Mater.,* 2019, **9**, 1901940.
24 J. He, G. Hartmann, M. Lee, G. S. Hwang, Y. Chen and A. Manthiram, *Energy Environ. Sci.*, 2019, **12**, 344-350.
25 W. Tian, B. Xi, Z. Feng, H. Li, J. Feng and S. Xiong, *Adv. Energy Mater.*, 2019, **9**, 1901896.
26 J. Zheng, J. Tian, D. Wu, M. Gu, W. Xu, C. Wang, F. Gao, M. H. Engelhard, J. G. Zhang, J. Liu and J. Xiao, *Nano Lett.*, 2014, **14**, 2345-2352.
27 S. Zhou, S. Yang, X. Ding, Y. Lai, H. Nie, Y. Zhang, D. Chan, H. Duan, S. Huang and Z. Yang, *ACS Nano*, 2020, **14**, 7538-7551.
28 L. Xu, H. Zhao, M. Sun, B. Huang, J. Wang, J. Xia, N. Li, D. Yin, M. Luo, F. Luo, Y. Du and C. Yan, *Angew. Chem.-Int Edit.*, 2019, **58**, 11491-11496.
29 M. Zhao, H. J. Peng, Z. W. Zhang, B. Q. Li, X. Chen, J. Xie, X. Chen, J. Y. Wei, Q. Zhang and J. Q. Huang, *Angew. Chem.-Int. Edit.*, 2019, **58**, 3779-3783.
30 H. Pan, J. Chen, R. Cao, V. Murugesan, N. N. Rajput, K. S. Han, K. Persson, L. Estevez, M. H. Engelhard, J.-G. Zhang, K. T. Mueller, Y. Cui, Y. Shao and J. Liu, *Nat. Energy*, 2017, **2**, 813-820.
31 R. Ma and T. Sasaki, *Adv. Mater.*, 2010, **22**, 5082-5104.
32 L. Wang and T. Sasaki, *Chem. Rev.*, 2014, **114**, 9455-9486.
33 S. Z. Butler, S. M. Hollen, L. Cao, Y. Cui, J. A. Gupta, H. R. Gutiérrez, T. F. Heinz, S. S. Hong, J. Huang, A. F. Ismach, E. Johnston-Halperin, M. Kuno, V. V. Plashnitsa, R. D. Robinson, R. S. Ruoff, S. Salahuddin, J. Shan, L. Shi, M. G. Spencer, M. Terrones, W. Windl and J. E. Goldberger, *ACS Nano*, 2013, **7**, 2898-2926.

34 V. Nicolosi, M. Chhowalla, M. G. Kanatzidis, M. S. Strano and J. N. Coleman, *Science*, 2013, **340**, 1226419.
35 R. Ma and T. Sasaki, *Accounts Chem. Res.,* 2015, **48**, 136-143.
36 T. Ali and C. Yan, *ChemSusChem*, 2020, **13**, 1447-1479.
37 Q. Shao, Z.-S. Wu and J. Chen, *Energy Storage Mater.*, 2019, **22**, 284-310.
38 S. B. Patil, H. J. Kim, H.-K. Lim, S. M. Oh, J. Kim, J. Shin, H. Kim, J. W. Choi and S.-J. Hwang, *ACS Energy Lett.*, 2018, **3**, 412-419.
39 H. Xu, S. Yang and B. Li, *J. Mater. Chem. A*, 2020, **8**, 149-157.
40 G. Chen, X. Song, S. Wang, X. Chen and H. Wang, *J. Power Sources*, 2018, **408**, 58-64.
41 D. R. Deng, F. Xue, C. D. Bai, J. Lei, R. Yuan, M. S. Zheng and Q. F. Dong, *ACS Nano*, 2018, **12**, 11120-11129.
42 A. K. Geim and I. V. Grigorieva, *Nature*, 2013, **499**, 419-425.
43 N. Sakai, K. Fukuda, Y. Omomo, Y. Ebina, K. Takada and T. Sasaki, *The J. Phys. Chem. C*, 2008, **112**, 5197-5202.
44 E. Coronado, C. Martí-Gastaldo, E. Navarro-Moratalla, A. Ribera, S. J. Blundell and P. J. Baker, *Nat. Chem.*, 2010, **2**, 1031-1036.
45 B.-W. Li, M. Osada, T. C. Ozawa, Y. Ebina, K. Akatsuka, R. Ma, H. Funakubo and T. Sasaki, *ACS Nano*, 2010, **4**, 6673-6680.
46 M. Osada, T. Sasaki, K. Ono, Y. Kotani, S. Ueda and K. Kobayashi, *ACS Nano*, 2011, **5**, 6871-6879.
47 N. Sakai, K. Kamanaka and T. Sasaki, *J. Phys. Chem. C*, 2016, **120**, 23944-23950.
48 X. Cai, L. Yin, N. Sakai, D. Liu, C. Teng, Y. Ebina, R. Ma and T. Sasaki, *ACS Appl. Nano Mater.*, 2019, **2**, 6378-6386.
49 M. Bai, X. Liu, T. Sasaki and R. Ma, *Nanoscale*, 2021, DOI: 10.1039/D0NR08824B.
50 R. Ma, X. Liu, J. Liang, Y. Bando and T. Sasaki, *Adv. Mater.*, 2014, **26**, 4173-4178.
51 W. Ma, R. Ma, C. Wang, J. Liang, X. Liu, K. Zhou and T. Sasaki, *ACS Nano*, 2015, **9**, 1977-1984.
52 X. Cai, N. Sakai, T. C. Ozawa, A. Funatsu, R. Ma, Y. Ebina and T. Sasaki, *ACS Appl. Mater. Interfaces*, 2015, **7**, 11436-11443.
53 W. Ma, R. Ma, J. Wu, P. Sun, X. Liu, K. Zhou and T. Sasaki, *Nanoscale*, 2016, **8**, 10425-10432.
54 P. Xiong, R. Ma, N. Sakai and T. Sasaki, *ACS Nano*, 2018, **12**, 1768-1777.
55 P. Xiong, X. Zhang, H. Wan, S. Wang, Y. Zhao, J. Zhang, D. Zhou, W. Gao, R. Ma, T. Sasaki and G. Wang, *Nano Lett.*, 2019, **19**, 4518-4526.
56 X. Lu, N. Sakai, D. Tang, X. Li, T. Taniguchi, R. Ma and T. Sasaki, *ACS Appl. Mater. Interfaces*, 2020, **12**, 33083-33093.
57 J. Jiang, Y. Li, J. Liu, X. Huang, C. Yuan and X. W. Lou, *Adv. Mater.*, 2012, **24**, 5166-5180.
58 P. Xiong, Y. Wu, Y. Liu, R. Ma, T. Sasaki, X. Wang and J. Zhu, *Energy Environ. Sci.*, 2020, **13**, 4834-4853.
59 P. Xiong, B. Sun, N. Sakai, R. Ma, T. Sasaki, S. Wang, J. Zhang and G. Wang, *Adv. Mater.*, 2020, **32**, 1902654.
60 P. Xiong, R. Ma, G. Wang and T. Sasaki, *Energy Storage Mater.*, 2019, **19**, 281-298.
61 B.-W. Li, M. Osada, Y. Ebina, S. Ueda and T. Sasaki, *J. Am. Chem. Soc.*, 2016, **138**, 7621-7625.
62 X. Cai, R. Ma, T. C. Ozawa, N. Sakai, A. Funatsu and T. Sasaki, *Nanoscale*, 2014, **6**, 14419-14427.
63 S. Ida, Y. Sonoda, K. Ikeue and Y. Matsumoto, *Chem. Comm.*, 2010, **46**, 877-879.
64 L. Li, R. Ma, Y. Ebina, K. Fukuda, K. Takada and T. Sasaki, *J. Am. Chem. Soc.*, 2007, **129**, 8000-8007.
65 P. Xiong, X. Zhang, F. Zhang, D. Yi, J. Zhang, B. Sun, H. Tian, D. Shanmukaraj, T. Rojo, M. Armand, R. Ma, T. Sasaki and G. Wang, *ACS Nano*, 2018, **12**, 12337-12346.
66 X. Cai, T. C. Ozawa, A. Funatsu, R. Ma, Y. Ebina and T. Sasaki, *J. Am. Chem. Soc.*, 2015, **137**, 2844-2847.
67 T. Nakato, N. Miyamoto and A. Harada, *Chem. Commun.*, 2004, DOI: 10.1039/b309628a, 78-79.
68 K. Akatsuka, G. Takanashi, Y. Ebina, N. Sakai, M.-a. Haga and T. Sasaki, *J. Phys. Chem. Solids*, 2008, **69**, 1288-1291.
69 Y. Tian, G. Li, Y. Zhang, D. Luo, X. Wang, Y. Zhao, H. Liu, P. Ji, X. Du, J. Li and Z. Chen, *Adv. Mater.*, 2020, **32**, e1904876.
70 H. J. Peng, G. Zhang, X. Chen, Z. W. Zhang, W. T. Xu, J. Q. Huang and Q. Zhang, *Angew. Chem.-Int. Edit.*, 2016, **55**, 12990-12995.
71 F. Y. Fan, W. C. Carter and Y. M. Chiang, *Adv. Mater.*, 2015, **27**, 5203-5209.
72 X. Liang, C. Hart, Q. Pang, A. Garsuch, T. Weiss and L. F. Nazar, *Nat. Commun.*, 2015, **6**, 5682.
73 X. Liang, A. Garsuch and L. F. Nazar, *Angew. Chem.-Int. Edit.*, 2015, **54**, 3907-3911.
74 X. Liang, Y. Rangom, C. Y. Kwok, Q. Pang and L. F. Nazar, *Adv. Mater.*, 2017, **29**, 1603040.
75 Y. Chen, H. Zhang, X. Yang, K. Feng, X. Li and H. Zhang, *RSC Adv.*, 2016, **6**, 81950-81957.
76 A. Ferrari, J. Robertson, S. Reich and C. Thomsen, *Phil. Trans. R. Soc. A.*, 2004, **362**, 2271-2288.
77 W. Xu, N. Mao and J. Zhang, *Small*, 2013, **9**, 1206-1224.
78 A. T. Ward, *The Journal of Physical Chemistry*, 1968, **72**, 744-746.
79 R. L. Aggarwal, L. W. Farrar and D. L. Polla, *J. Raman Spectrosc.*, 2011, **42**, 461-464.
80 Z. Wang, J. Shen, J. Liu, X. Xu, Z. Liu, R. Hu, L. Yang, Y. Feng, J. Liu, Z. Shi, L. Ouyang, Y. Yu and M. Zhu, *Adv. Mater.*, 2019, **31**, e1902228.
81 X. Yang, X. Gao, Q. Sun, S. P. Jand, Y. Yu, Y. Zhao, X. Li, K. Adair, L. Y. Kuo, J. Rohrer, J. Liang, X. Lin, M. N. Banis, Y. Hu, H. Zhang, X. Li, R. Li, H. Zhang, P. Kaghazchi, T. K. Sham and X. Sun, *Adv. Mater.*, 2019, **31**, e1901220.

This journal is © The Royal Society of Chemistry 20xx

Please do not adjust margins